

# Controllable hydrothermal growth of $\text{Fe}_2\text{O}_3/\text{GO}$ wrapped nano-composites and its sustainable applications

**M. R. Abhilash<sup>a</sup> & S. Srikantaswamy<sup>a,b\*</sup>**

<sup>a</sup> Advanced Materials Laboratory, Department of Studies in Environmental Science, University of Mysore, Manasagangotri, Mysuru 570006, India.

<sup>b</sup> Centre for Materials Science and Technology, Vijnana Bhavan, University of Mysore, Manasagangotri, Mysuru 570006, India.

Received: September 03, 2018

Accepted: October 26, 2018

## ABSTRACT

We report the synthesis of a new range of iron oxide-graphene and nano-composites at different reaction temperatures for improved photocatalytic and biological application purposes. Effectively synthesized by hydrothermal method, a graphene sheet is prepared by modified Hummer's method and was wrapped to iron oxide surface. Further insights into the nanoparticles, chemical composition, morphology and micro-structural features of the materials were characterized by X-ray diffractometer, Fourier transform infrared spectroscopy, Dynamic light scattering, Scanning electron microscopy, Energy dispersive spectroscopy, BET surface area and X-ray spectroscopy, etc. The nanoparticles were found to have crystalline iron oxides with a mixture of magnetite and maghemite crystalline phases with graphene wrap. Magnetic analysis by vibrating sample magnetometer showed that the nanoparticles are ferrimagnetic. The structural and magnetic properties of the nanoparticles are found to be dependent on the nanoparticle sizes which are substantially affected by the reaction temperature and particular time lag. A range of environmental clean-up technologies have been proposed for wastewater treatment which applied iron oxide composite with graphite oxide wrapped nanomaterials act as nanosorbents and photocatalysts. Moreover, iron oxide and graphene-based immobilization technology for enhanced removal efficiency tend to be an innovative research point. This work is outlined the latest applications of  $\text{Fe}_2\text{O}_3/\text{GO}$  nano-materials with different temperature for wastewater treatment, photocatalysis, bacterial degradation and biological screening applications.

**Keywords:** Iron oxide; Nano particles; Tuberculosis; Bacterial degradation; Cytotoxicity

## 1. Introduction

Iron oxides are common compounds, which are widespread in nature and can also be readily synthesized in the laboratory. Magnetic iron oxides have served humans for centuries, for example, the application of small iron oxide nanoparticles (IONPs) as a contrast agent for *in-vitro* diagnostics has been practiced for nearly half a century [1]. In the past decade, the synthesis of magnetic IONPs has been intensively developed not only for its fundamental scientific interest but also for its many technological applications, such as targeted drug delivery, bio-separation, and environmental applications [2]. Particularly, bio-applications based on magnetic nano-particles (NPs) have received considerable attention because NPs offer unique advantages over other materials. For example, magnetic IONPs are inexpensive to produce, physically and chemically stable, biocompatible, and environmentally safe [3]. To understanding the correlation between the magnetic properties and the size and shape of IONPs is a prerequisite for widespread applications of magnetism in data storage, bio-separation, medicine and environment clean-up procedures [4]. Due to its unique two-dimensional one-atom-thick sheet structure with high surface area and abundant oxygen-containing functionalities, Graphene oxide (GO) can be prepared easily from abundant graphite by oxidization and reduced graphene oxide (RGO) prepared by subsequent reduction of GO have recently received enormous interest for environmental remediation applications [5]. The hydrothermal technique provides an excellent possibility for processing the advanced materials whether as bulk single crystals or fine particles, or nanoparticles owing to a highly controlled diffusion in a closed system under mild temperature pressure conditions that are cost-effective with a high yield of products and excellent particle structure [6]. This method is effectively utilized used to prepare nano-composites. To the best of our knowledge, there are still no reports on the successful combination of controllable  $\text{Fe}_2\text{O}_3/\text{GO}$  and its impact on the photocatalytic degradation of Rhodamine B (RB) and Janus green (JG), similarly, Heavy metals like Lead (Pb); Chromium (Cr) and Mercury (Hg); Cobalt (Co) and also, some biological applications like bacterial degradation and for the first time we are reporting the excellent anti-M. Tuberculosis activity by using wrapped  $\text{Fe}_2\text{O}_3/\text{GO}$  controllable nano-composites and cytotoxicity studies. Tackling the above issues, we report in this paper the synthesis of a range of cost-effective wrapped nano-composites for various

applications. The key to the enhanced adsorption capacity is the unique loading of primarily amorphous iron oxide nanoparticles of high specific surface area on GO. The composite adsorbents have been designed to contain different contents of the amorphous iron oxide; our results suggest their high potential as cost-effective adsorbents for various eco-friendly applications.

## 2. Material and methods

### 2.1. Chemicals

Natural graphite flake (+100 mesh: ≥75.5%, Sigma-Aldrich), potassium permanganate (99.0+%, Sigma Aldrich), hydrogen peroxide (50%, Fisher Scientific), sulfuric acid (96.9 wt%, Fisher Scientific), phosphoric acid (85+%, Acros), ferrous sulfate heptahydrate (99+%, Sigma Aldrich), ferric sulfate hydrate (97%, Fe 21.6%, Sigma Aldrich), ammonium hydroxide solution (28–30%, Sigma Aldrich), hydrochloric acid (37%, Fisher Scientific), methanol (ACS reagent, Fisher Scientific), were used as received without any additional purification. Ferrous chloride tetrahydrate ( $\text{FeCl}_2 \cdot 4\text{H}_2\text{O}$  Merck>99 %), ferric chloride hexahydrate ( $\text{FeCl}_3 \cdot 6\text{H}_2\text{O}$  Merck>99 %), salts, and ammonium hydroxide ( $\text{NH}_4\text{OH}$  Merck, 25 % of ammonia) were used for the synthesis of iron oxide nanoparticles. All chemicals were of reagent grade and used without further purification, de-ionized water was purified by a Barnstead/Synbron Nanopure II purification system.

### 2.2. Synthesis of graphene oxide (GO)

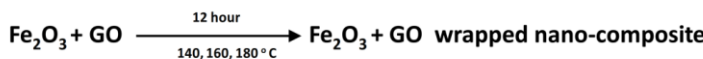
GO was synthesized by exfoliation of natural graphite flakes with the development of sophisticated Hummers method with slight modifications reported by Tour *et al* [7]. In a typical process, a mixture of concentrated  $\text{H}_2\text{SO}_4/\text{H}_3\text{PO}_4$  (360:40 mL) was prepared in a round-bottom flask, and then 3 g of graphite flakes were added to the mixture under vigorous mechanic stirring for 10 min to obtain a dark colored suspension. Subsequently, 18 g of  $\text{KMnO}_4$  were added slowly into the above suspension in an ice bath. The mixture was stirred vigorously for 36 h at 50 °C. A reddish brown viscous mixture was obtained. This mixture was cooled to room temperature, and then poured slowly into 400 mL of cold deionized water containing 3 mL of  $\text{H}_2\text{O}_2$  (50%). Afterwards, the suspension was centrifuged and washed sequentially with HCl, water, and then methanol for several times, until pH reached 6. The solid material was collected after centrifugation and dispersed again in 1200 mL of water as the stock solution (GO concentration of 3.5 mg  $\text{mL}^{-1}$ , 4.2 g in total) for subsequent use.

### 2.3. Hydrothermal Preparation of $\text{Fe}_2\text{O}_3$

The hydrothermal technique has been found to be one of the best techniques to prepare  $\text{Fe}_2\text{O}_3/\text{GO}$  nano-particles of desired size with homogeneity in composition and high degree crystalline particles. The primary nano-particles were synthesized using hydrothermal method. Then for the growth of these nano-particles, hydrothermal treatment was used. For this reason,  $\text{FeCl}_3$  and  $\text{NaOH}$ , Ammonia (Aldrich, India) (37.5 mol)  $\text{FeCl}_3 \cdot 6\text{H}_2\text{O}$  and (37.5 mmol)  $\text{FeCl}_2 \cdot 4\text{H}_2\text{O}$  were dissolved into 25 ml of distilled water. 25mL of 25 % ammonia was added to the salt solution under stirring condition at 700 rpm for 2 min right after 15 ml of mixture was put into a Teflon-lined stainless Morey autoclave, and the autoclave was heated to 140, 160, and 180 °C in an oven and maintained at 12 h reaction time. Moreover, the influence of reaction temperature on the product was investigated. Temperature plays a crucial role in the formation of well-defined spherical product. Autoclave was naturally cooled to room temperature, and the precipitates were washed with distilled water and isolated under magnet. The final products were dried at 60 °C and were ready for characterization.

### 2.4. Graphene oxide (GO) wrapped (or) composite to $\text{Fe}_2\text{O}_3$ surface

GO was synthesized through a Hummer's method with slight modifications, and iron oxide was synthesized from hydrothermal method as follows: (the molar ratio of  $\text{Fe}_2\text{O}_3$ : GO is fixed at 1: 0.05 to retain the magnetic) 1.586 g of  $\text{Fe}_2\text{O}_3$  and 0.120 g of GO were dispersed in 50 mL of  $\text{CHCl}_3$  and sonicated for 60 min. Then, the suspension was stirred at room temperature for 12 h. After that, the mixture was filtered and dried at 80 °C for 5 h.



The initial composites used are super paramagnetic at room temperature, and saturation magnetization,  $M_s$  of nanoparticles was 69.2 emu/g and saturation field,  $H_s$  was 9,854 Oe. And the crystal diameters,  $d_{XRD}$  of the initial nanoparticles synthesized by hydrothermal method are 9 nm.

## 2.5 Characterizations and measurements

Magnetic measurement was performed with a vibration sample magnetometer (VSM, ADE EV9 Model). Magnetization curves were measured at room temperature in a maximum magnetic field of  $\pm 20$  kOe with 10e intervals. Braunauer-Emmett-Teller (BET) specific surface area, pore volume, and pore size distribution of the samples were determined by N<sub>2</sub> sorption at 77 K using a Micromeritics ASAP 2020 physico-sorption analyzer. Before the sorption measurements, the samples were degassed under vacuum at 100°C for at least 12 h. The samples were run in a standard mode. Ultima III Series, RIGAKU, TSX System, Japan with Cu radiation (wavelength 1.54° Å) at room temperature. were used for wide-angle X-ray diffraction (XRD) patterns of the Fe<sub>2</sub>O<sub>3</sub>-GO nano-composites. Scanning electron microscopic (SEM) images of the Fe<sub>2</sub>O<sub>3</sub>-GO composites was captured using HITACHI (S-3400 N, Japan) with 10 kV acceleration voltages. For image analysis, the composites were placed on a carbon-coated copper in a tiny amount and allowed to air dry and images of nanoparticles were taken. The Energy Dispersive Spectroscopy (EDS) analysis was carried out using HITACHI (Noran System 7, USA) system attached to SEM for the detection of composite nanoparticles. Fourier-transformed infrared (FTIR) spectra were obtained on a Thermo Scientific Nicolet 6700 Analytical FTIR spectrometer. The samples were prepared as pel-lets using spectroscopic-grade KBr. Zeta potential measurements of the dilute dispersions (0.1 mg mL<sup>-1</sup>) of the various Fe<sub>2</sub>O<sub>3</sub>-GO composites were performed with a Brookhaven Nano-Brook Omni Instrument at 25 °C. The particle size distribution (PDS) and zeta potential of Iron oxide-GO nano-particle were monitored by using Microtrac (USA) particle size analyzer. The analyzer provides the size measurement and confirmation of particle size distribution. The concentration of heavy metals was measured with Inductively Coupled Plasma Atomic Emission Spectroscopy techniques (ICP-AES) using the Perkin-Elmer Optima 8000, ICP-OES.

## 2.6. Determination of antibacterial activity of Fe<sub>2</sub>O<sub>3</sub>-GO: 140°C, Fe<sub>2</sub>O<sub>3</sub>-GO: 160°C, Fe<sub>2</sub>O<sub>3</sub>- GO: 180°C controllable composites.

The antibacterial screening of Fe<sub>2</sub>O<sub>3</sub>-GO: 140°C, Fe<sub>2</sub>O<sub>3</sub>-GO: 160°C, Fe<sub>2</sub>O<sub>3</sub>-GO: 180°C nano-composites along with control by disc diffusion method [8, 9], against Gram-positive (*Bacillus subtilis*, MTCC 121 and *Staphylococcus aureus* MTCC 7443) and Gram-negative (*Escherichia coli*, MTCC 7410 and *Pseudomonas aeruginosa* sp., MTCC 733) bacteria. About 100 µL of the test bacteria ( $1.5 \times 10^8$  CFU mL<sup>-1</sup>) were seeded uniformly onto the surface of nutrient agar (NA) media using a sterile glass spreader. The sterile discs (6 mm) were loaded with 50 µL of Fe<sub>2</sub>O<sub>3</sub>-GO controllable composites (1 mg disc<sup>-1</sup>) individually and placed equidistantly on NA plates along with respective controls. The inoculated plates were incubated at 37 ± 2 °C for 24 h and zone of inhibition around the discs were measured [9]. Further the Live and dead cell analysis was performed to distinguish dead and viable bacterial cells upon treatment with Fe<sub>2</sub>O<sub>3</sub>-GO-NPs following the method of Chen *et al* [10] with minor modifications. About 100 µL bacterial cell suspensions were treated with 50 µL of Fe<sub>2</sub>O<sub>3</sub>-GO-NPs (100 µg) were mixed and incubated at 37 ± 2 °C for 24 h, untreated bacteria served as control. After incubation, the mixture was centrifuged at 5000 rpm for 5 min at 4 °C and the pellet was washed thrice with phosphate buffer saline (PBS). Each of the samples obtained was mixed with fluorescent dye solution of ethidium bromide (EB) and acridine orange (AO) at 1:1 ratio and incubated for 30 min. After rinsing with PBS, about 5 µL of cell suspension was trapped in between glass slide and cover slip and examined using a Fluorescence microscope (Lawrence and Mayo, Germany).

## 2.8. Photocatalytic experiments of degradation of dyes

The photocatalytic activities of the synthesized materials were evaluated by the degradation of Rhodamine B (RB) and Janus green (JG) dyes (200 mL of aqueous solution of the dyes ( $1 \times 10^{-5}$  mol L<sup>-1</sup>) under UV light radiation. The light source used was a 150 W, Xe (Xenon) lamp and the distance between the UV source and the photoreaction vessel was 10 cm. Prior to irradiation, the suspensions were magnetically stirred in the dark for 30 min and further the photoreaction vessel was exposed to UV irradiation under ambient conditions. Different concentrations of dyes (10 ppm, 20 ppm, and 30 ppm) were considered for performing the photodegradation experiment with 10 mg of catalyst nanoparticles. At regular time intervals, 3 mL of the suspension was taken for centrifugation to separate the photocatalyst and further evaluated using a UV-Vis absorption spectrometer. The photodegradation efficiency percentage is calculated from the equation given below %.The photodegradation efficiency percentage is calculated from the equation given below;

$$\% \text{ Photodegradation efficiency} = C_0 - C / C_0 \times 100$$

∴ Where C<sub>0</sub> = initial concentration of dye and C = concentration of dye after photo irradiation (final).

## 2.9. Photocatalytic removal of heavy metals

The removal of heavy metals was observed by analyzing the concentration of different heavy metals present in effluent. In this experiment we carried out stirring to clear determination of photocatalytic Research Paper

activity for different  $\text{Fe}_2\text{O}_3$ -GO: 140°C,  $\text{Fe}_2\text{O}_3$ -GO: 160°C, and  $\text{Fe}_2\text{O}_3$ -GO: 180°C controllable composite in effluent. The heavy metal concentration was analyzed for the supernatant solution after centrifugation using ICP-AES) using the Perkin-Elmer Optima 8000, ICP-OES. The comparison was made by using values obtained after and before treatment. In figure.7, Heavy Metal removal studies in two different industrial effluent used for the study, specific effluent contains Lead (Pb); Chromium (Cr), respectively, the initial concentration of Lead was 1.398 mg/L<sup>-1</sup> and Chromium is 1.897 mg/L<sup>-1</sup>. Other industrial effluent specifically contains Mercury (Hg); and Cobalt (Co), initial concentration of Mercury 1.211 mg/L<sup>-1</sup> and Cobalt is 1.351 mg/L<sup>-1</sup> by using for photocatalytic removal of heavy metals.  $\text{Fe}_2\text{O}_3$ /GO: 140 °C, 160 °C and 180 °C nano-composites shows a very encouraging results in the case of heavy metal removal from the aqueous solution of effluent by filtrations.

#### 2.10. Anti-TB activity

The anti-mycobacterial activity of compounds were assessed against *Mycobacterium tuberculosis* using microplate Alamar Blue assay (MABA). This methodology is non-toxic, uses a thermally stable reagent and shows good correlation with proportional and BACTEC radiometric method. Briefly, 200 $\mu$ l of sterile deionized water was added to all outer perimeter wells of sterile 96 wells plate to minimized evaporation of medium in the test wells during incubation. The 96 wells plate received 100  $\mu$ l of the Middle-brook 7H9 broth and serial dilution of compounds was made directly on plate. The final drug concentrations tested were 100 to 0.2  $\mu$ g/ml. Plates were covered and sealed with parafilm and incubated at 37°C for five days. After this time, 25 $\mu$ l of freshly prepared 1:1 mixture of Almar Blue reagent and 10% tween 80 was added to the plate and incubated for 24 hrs. A blue color in the well was interpreted as no bacterial growth, and pink color was scored as growth. The MIC was defined as lowest drug concentration which prevented the color change from blue to pink [11].

#### 2.11. Normal Cell line toxicity testing using HEK-293

HEK-293 (human embryonic kidney), cell lines were obtained from the American Type Culture Collection, USA. The growth media: RPMI-1640, sufficient minimum essential medium (MEM), and the phosphate buffer solution (PBS) tablets were obtained from Sigma Chemical Co., St Louis, USA. Standard quality fetal calf serum, penicillin-streptomycin, and trypsin were obtained from Sigma labs. The XTT kit, which consists of the 2, 3-bis (2-methoxy-4-nitro-5-sulfophenyl)-5-[(phenylamino) carbonyl]-2H-tetrazolium hydroxide (XTT) labeling reagent and the solubilisation solution was procured from Sigma labs, USA. Trypsin (0.25% + EDTA, 1 mM in PBSA), XTT dye-50 mg/mL, sterilized Sorensen's glycine buffer (0.1 M glycine, 0.1 M NaCl adjusted to pH 10.5 with 1 M Na OH), DMSO, growth medium is procured from Aldrich labs. XTT labeling reagent and electron-coupling reagent were thawed, respectively, in a water bath at 37°C. Each vial was mixed systematically to obtain a clear solution. To achieve a cell proliferation assay (XTT) with one microplate (96 wells), 5 mL XTT labeling reagent was mixed with 0.1 mL electron-coupling reagent were used. Cells were grown in 96-well plates in a final volume of 100  $\mu$ L of culture medium per well. Each well contained 1  $\times$  10<sup>5</sup> cells/mL and was incubated for 24 h in a 5% CO<sub>2</sub> incubator at 37°C. As described above, the same procedure was adopted for cell culture. The HEK-293 cell line was used as it has the lowest IC<sub>50</sub> (the concentration of test compound that can inhibit 50% of the normal cells from proliferating) for functionalized  $\text{Fe}_2\text{O}_3$ -GO composite nanoparticles and the same was observed using microscope. The cells were treated with different nanoparticles at a concentration that was similar to the IC<sub>50</sub> value. The plate was then incubated again in the 5% CO<sub>2</sub> incubator at 37°C for 48 h. The untreated cells (control) were also incubated for 48 h. The growth of the cells was photographed using a phase contrast microscope (Olympus, USA). Cells, grown in a 96-well tissue culture plate, are incubated with the yellow XTT solution (0.3 mg/mL) for additional 4 h. The cells were grown till they become turbid and confluent. Trypsin was then added to the cells to prepare a cell suspension, and the number of viable cells was counted with a hemocytometer. Fifty microliters of suspension containing 1  $\times$  10<sup>5</sup> cells was seeded in each well of a 96-well microtiter plate. The plate was then incubated overnight at 37°C with 5% CO<sub>2</sub>. Periodically, the medium was replaced. A 96-well micrometer plates are used for this experiment. Two hundred microliters of MEM is added in the required number of wells; to this, 50  $\mu$ L of different cell lines are added in each well.  $\text{Fe}_2\text{O}_3$ -GO composites of different concentrations (10 $\mu$ g/ml) were administered into the wells separately. The cells were cultured in the appropriate medium, supplemented with 5–10% fetal calf serum and 1% penicillin-streptomycin, using 25 cm<sup>2</sup> flasks in a 37°C incubator with 5% CO<sub>2</sub>. To subculture the cells, the cells were separated, and the fresh culture medium was used with fresh medium as follows: in the first step, the old medium was removed, and then the cells were rinsed briefly with PBS to wash the cells. After this, 1–2  $\mu$ L of trypsin was added, and the flask was incubated at 37°C and 5% CO<sub>2</sub> for 5 min. The upper part of the liquid is discarded, and the remaining detached cells, present in the lower part of the flask, are taken in a

separate flask; 20  $\mu\text{L}$  of medium was added, and the culture was divided in two parts. One part of this was transferred to a new flask.

## 2.12. Statistical analysis

Data from three replicates were analyzed for each experiment and analysis of variance (ANOVA) using SPSS Inc. 16.0. Significant effects of treatments were determined by F values ( $p \leq 0.05$ ). Tukey's HSD test separated treatment means.

## 3. Results and discussion

### 3.1. Characterization results of synthesized $\text{Fe}_2\text{O}_3/\text{GO}$ controllable nano-composites

To structurally characterize the samples, the XRD measurements were carried out at  $2\theta = 10^\circ\text{--}70^\circ$ . Figure 1 shows the XRD spectra of GO,  $\text{Fe}_2\text{O}_3$ -GO, 140°C,  $\text{Fe}_2\text{O}_3$ -GO, 160°C,  $\text{Fe}_2\text{O}_3$ -GO, 180°C. In the spectrum of GO, within a strong peak at  $12^\circ$  arising from the interlayer spacing between stacked GO sheets [7]. This peak is absent in  $\text{Fe}_2\text{O}_3$ -GO: 140°C,  $\text{Fe}_2\text{O}_3$ -GO: 160°C due to the complete exfoliation of GO sheets by iron oxide. In addition, a very weak and broad peak is also noticed near  $43^\circ$  (indicated by arrows) in the spectrum of GO, which is attributed to the (1 0 0) peak of graphitic structures [12]. The iron oxide shows sharp strong diffraction peaks matching well those of  $\text{Fe}_3\text{O}_4$  (JCPDS Card #75-0033) or  $\gamma\text{-Fe}_2\text{O}_3$  (JCPDS Card #39-1346), which have similar XRD patterns. It is observed that the peak intensities increased and the wideness of the peaks decreased as the reaction temperature and time increased. The average crystallite size ( $L$ ) is evaluated from the full width at half maximum of the (3 1 1) peak at  $2\theta = 35.5^\circ$  according to the Scherrer equation and presented in Table 1. The dXRD of nanoparticles synthesized at 140, 160, and 180 °C for 12 h were calculated to be 13, 15, and 17 nm, respectively. The increase of the reaction temperature increased the nanoparticle size. This is in a good agreement with Taniguchi et al.'s report [13].

Magnetic data are listed in Table 1. All the respective samples are ferromagnetic in nature. When the reaction temperatures were 140, 160, and 180 °C, the  $M_s$  Values were 81.0, 78.2, and 75.6 emu/g and the  $H_s$  values were 8.158, 8.651, and 8.452 Oe, respectively. And the values of  $H_c$ , was in the same order of reaction temperature as 89, 72, and 38 Oe, respectively. It is observed that the increase of the nanoparticle size with increasing temperature resulted in an increase of  $M_s$  and  $H_c$  and decrease of  $H_s$ . At this reaction temperature and times, the large particle sizes were obtained, see Table 1. with the increase of the nanoparticle size. The FT-IR analysis also disclosed that the shoulders in the 600–750  $\text{cm}^{-1}$  wakened and then disappeared for sample 9 due to the only magnetite phase [14]. Magnetite is very unstable and is sensitive to oxidation and therefore easily transforms to maghemite in the presence of oxygen [15]. Consequently, the increase of  $M_s$  with increasing nanoparticle size is probably due to the decrease of the degree of the oxidization on the particles due to the small surface area. Present study, the same trend of changes on  $H_c$  values of  $\text{Fe}_2\text{O}_3/\text{GO}$  nano-composites was observed. Consequently, our results showed that the reaction temperature and times have substantial effect on structural and magnetic properties and hence nanoparticle size.

FTIR spectra of GO,  $\text{Fe}_2\text{O}_3$ , and  $\text{Fe}_2\text{O}_3/\text{GO}$  controllable composites are shown in Figure 2. The spectrum of GO shows C O (1729  $\text{cm}^{-1}$ ), aromatic C C (1620  $\text{cm}^{-1}$ ), carboxyl O=C-O (1400  $\text{cm}^{-1}$ ), epoxy C-O (1225  $\text{cm}^{-1}$ ), and alkoxy C-O (1053  $\text{cm}^{-1}$ ) stretching vibrations [16]. The spectrum of iron oxide sample shows two broad bands in the low frequency region (750–400  $\text{cm}^{-1}$ ), corresponding to the Fe-O vibration in  $\text{Fe}_3\text{O}_4$  [17]. The infrared spectra of GO,  $\text{Fe}_2\text{O}_3$ -GO: 140°C,  $\text{Fe}_2\text{O}_3$ -GO: 160°C,  $\text{Fe}_2\text{O}_3$ -GO: 180°C and the iron oxide, show a broadband with the peak maximum at 1578  $\text{cm}^{-1}$ , corresponding to aromatic C C stretch in GO [18]. Other bands arising from GO become indefinite inside the composites due to its lowered content. In  $\text{Fe}_2\text{O}_3$ -GO: 140°C, the presence of iron oxide can be confirmed from the bands at 552  $\text{cm}^{-1}$  and 442  $\text{cm}^{-1}$ .  $\text{Fe}_2\text{O}_3$ -GO: 160°C and  $\text{Fe}_2\text{O}_3$ -GO: 180°C show also analogous spectral characteristics with more or less differences in the absorption intensities in the low wave number range due to the irrelatively lowered iron oxide content.

The GO,  $\text{Fe}_2\text{O}_3$ -GO: 140°C,  $\text{Fe}_2\text{O}_3$ -GO: 160°C,  $\text{Fe}_2\text{O}_3$ -GO: 180°C and the iron oxide control sample controllable composites, along with GO and the iron oxide control sample, were further characterized with  $N_2$  sorption analysis at 77 K for their textural properties. Figure 3 summarizes the characterization data, including surface area, pore volume, and average meso/macro-pore size. This indicates these samples contain both micropores and mesopores.

The iron oxide control sample instead shows only a slight uptake at the low relative pressure end ( $P/P_0 < 0.05$ ), and a sharp uptake with an H-3 type hysteresis loop at high relative pressure end ( $P/P_0 > 0.9$ ) [19], indicating that the sample contains predominantly large mesopores and/or macropores (average size: 28 nm). In this sample, the mesopores/macropores should be the bury nanoparticle pores resulting from the

aggregation of the crystalline  $\text{Fe}_2\text{O}_3$  nanoparticles. GO and the iron oxide control sample have a surface area of 126 and  $77 \text{ m}^2\text{g}^{-1}$ , respectively, and a pore volume of 0.11 and  $0.36 \text{ cm}^3\text{g}^{-1}$ , respectively as clearly tabulated in table 2. On the basis of its surface area and magnetite density ( $5.18 \text{ g cm}^{-1}$ ) [20]. The crystalline  $\text{Fe}_2\text{O}_3$  nanoparticles in the iron oxide control sample have an estimated average diameter of 16 nm, which is nearly identical to the average size estimated above from XRD the three composites show significantly enhanced surface area ( $327\text{--}341 \text{ m}^2\text{g}^{-1}$ ) and pore volume ( $0.20\text{--}0.29 \text{ cm}^3\text{g}^{-1}$ ). Meanwhile, both surface area and pore volume show slight increases with the increase of the iron oxide content from GO,  $\text{Fe}_2\text{O}_3\text{-GO}$ ,  $140^\circ\text{C}$ ,  $\text{Fe}_2\text{O}_3\text{-GO}$ ,  $160^\circ\text{C}$ ,  $\text{Fe}_2\text{O}_3\text{-GO}$ ,  $180^\circ\text{C}$  and the iron oxide control sample.

$\text{Fe}_2\text{O}_3\text{-GO}$ :  $140^\circ\text{C}$ ,  $\text{Fe}_2\text{O}_3\text{-GO}$ :  $160^\circ\text{C}$  and  $\text{Fe}_2\text{O}_3\text{-GO}$ :  $180^\circ$  Characterized by SEM, chemical composition and elemental analysis of the composites was investigated by EDS analysis, in that order. The SEM images of the GO wrinkled corrugated nanosheets were wrapped with  $\text{Fe}_2\text{O}_3$  as shown in figure. 6, at the same time as, the  $\text{Fe}_2\text{O}_3\text{-GO}$  shows the micro spherical shape of uniform surface structures GO are wrapped uniformly on the surface of iron oxide and the two-dimensional structure of graphene sheets with micrometer long wrinkles can be clearly distinguished as shown in Figure 5. The GO nanosheets function as conductive bands for the interconnection between various  $\text{Fe}_2\text{O}_3$  microspheres/isometric structures and the transfer of photogenerated charge carriers for enhancement of the photocatalytic efficiency. The graphene sheets play an important role in assisting as template/matrix for  $\text{Fe}_2\text{O}_3$  nanoparticle growth, its dispersion on its surface and at the same time  $\text{Fe}_2\text{O}_3$  decoration helps to prevent the aggregation of the graphene sheets. Energy dispersive spectrum of  $\text{Fe}_2\text{O}_3\text{-GO}$  nano-composites peaks are evident that, high-quality of  $\text{Fe}_2\text{O}_3\text{-GO}$  nano-composites. Similarly, SEM-EDS analysis has been carried out to know the morphology and quantitative estimation of controllable  $\text{Fe}_2\text{O}_3\text{-GO}$  composite as clearly showed and tabulated in Figure 6.

The histogram of Dynamic light scattering analysis for particle size distribution of controllable composites is depicted in Figure 6. DLS analysis is regarded as one of the reliable technique for evaluating particle size, distribution and zeta potential of nanoparticles in solution. the present analysis revealed the presence of particles with an average diameter of 74 nm in the aqueous colloidal solution. The surface charge (zeta potential) of the  $\text{Fe}_2\text{O}_3\text{-GO}$  controllable nanoparticles plays a vital role during the interaction with other biological system as well as environmental degradation systems. The particles examined presently possessed a zeta potential value of  $\text{Fe}_2\text{O}_3\text{-GO}$ :  $140^\circ\text{C}$  is  $-0.1 \text{ mv}$ ,  $\text{Fe}_2\text{O}_3\text{-GO}$ :  $160^\circ\text{C}$  is  $13.9 \text{ mv}$ , and finally,  $\text{Fe}_2\text{O}_3\text{-GO}$ :  $180^\circ\text{C}$  is  $-7.8 \text{ mV}$  was exclusively determined in present study. Nanoparticles with a zetapotential of  $-10$  and  $+10 \text{ mV}$  have a neutral charge, while if it is greater than  $+30 \text{ mV}$  or less than  $-30 \text{ mV}$ , it is considered to be strongly cationic and anionic, respectively [21]. Based on the results, the growth mechanisms of the  $\text{Fe}_2\text{O}_3\text{-GO}$  composites can be predicted. The  $\text{Fe}_2\text{O}$  positive ions gather on the negatively charged GO surface. The hydrothermal processes results in reaction of adsorbed  $\text{Fe}_2\text{O}_3$  on GO with responsible ions to generate the initial  $\text{Fe}_2\text{O}_3$  nuclei.

### 3.2. Determination of antibacterial activity of $\text{Fe}_2\text{O}_3\text{-GO}$ nano-composite

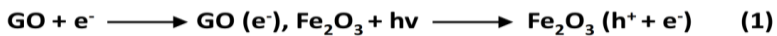
$\text{Fe}_2\text{O}_3\text{-GO}$ :  $140^\circ\text{C}$ ,  $\text{Fe}_2\text{O}_3\text{-GO}$ :  $160^\circ\text{C}$ ,  $\text{Fe}_2\text{O}_3\text{-GO}$ :  $180^\circ\text{C}$  were further tested for their potential to inhibit test bacterial pathogens by disc diffusion method Figure 7. The results of antibacterial activity showed a significant zone of inhibition against test pathogens (see table 3). It was noted that among the test samples,  $\text{Fe}_2\text{O}_3\text{-GO}$  controllable composites showed maximum inhibition zone of 23.24, 22.10 and 20.17 for *Staph. aureus*, *P. aeruginosa* and *E. Coli*, respectively, in  $\text{Fe}_2\text{O}_3\text{-GO}$ :  $180^\circ$  due its large surface area. In the case of *B. Subtilis*, only a trifling response to  $\text{Fe}_2\text{O}_3\text{-GO}$  nano-composite is observed, while there is no zone of inhibition in SDW (Sterile Distilled Water) diffused discs against test pathogens. Our study clearly suggests that  $\text{Fe}_2\text{O}_3\text{-GO}$  nano-composite inhibit bacterial pathogens by rupturing the outer and inner wall of the cell which leads to disorganization and leakage of the cell membrane are clearly evident in the Figure 8.

The morphological changes occurring during the inhibition of bacterial pathogens was carried out by selective staining of live and dead cells. Among the fluorescent nucleic acid dyes used, AO is known to stain both live and dead cells, while EB can penetrate only cells with compromised or damaged cell membranes.

### 3.3. Photodegradation mechanism of dyes and heavy metals

Hydrogen generation from photo-induced water decomposition is emerging as a viable option to simultaneously solve energy and environmental problems. Among various photo-induced  $\text{H}_2$  generation techniques, photocatalytic water splitting is promising because of the low cost and high sustainability features of the reaction system. The search for suitable catalysts to split water under irradiation has led to intensive studies [22, 23]. The photocatalytic degradation of organic dyes followed by heavy metals by using controllable  $\text{Fe}_2\text{O}_3\text{-GO}$  nanocomposite semiconductors under UV irradiation involves excitation of the semiconductors by light irradiation from photo-generated electrons in the conduction band and holes in the valence band and the subsequent chemical reactions within the surrounding media after the photo-

generated charges move to the particle surface. Moreover, based on the excitation of dyes and heavy metals in which act as a sensitizer of visible/UV light injects excited electrons to an electron acceptor to become a cationic/anion dye free radical followed by self-degradation or degradation by the reactive oxidation species [24]. The improved photodegradation efficiency of the Fe<sub>2</sub>O<sub>3</sub>-GO: 140°C, Fe<sub>2</sub>O<sub>3</sub>-GO: 160°C, Fe<sub>2</sub>O<sub>3</sub>-GO: An 180°C composite is attributed to the adsorption of contaminant molecules through catalysis, the light absorption and finally the charge separation and transportation. The optical quenching and surface resonance characteristics is higher. Fe<sub>2</sub>O<sub>3</sub> valence electrons are excited to the conduction band, thereby producing the electron-hole pairs. The photo-generated electrons are transferred to GO, which acts as an electron acceptor. GO promotes the interfacial electron transfer process and effectively hinders the recombination of the photo-generated electrons and holes. The holes in the valence band of iron oxide can react with absorbed hydroxyl groups to form surface hydroxyl radicals. in the interim, the photo-generated electrons on the surface of the composite nanoparticles, as well as the trapped electrons on GO, can also react with the dissolved oxygen to form reactive oxygen species, which further react with water to form hydroxyl radicals [25]. Both the hydroxyl radicals and holes can degrade and oxidize the dye molecule in systematic manner [26]. The heavy metals as, Lead (Pb), Chromium (Cr), Mercury (Hg) and Cobalt (Co) in two different industrial effluents were considered in the present study. Materials showed their own degradation efficiency to degrade of heavy metals in industrial effluent. Electron-hole pairs in the excited Fe<sub>2</sub>O<sub>3</sub> could be efficiently separated and the efficient transfer of photo induced electrons between Fe<sub>2</sub>O<sub>3</sub> and GO plays a vital role in degradation. The efficiency of the photocatalytic reaction significantly depends on the efficiency of adsorption of organic contaminants and heavy metals on the photocatalysts and the separation of the photo-generated electron-hole pairs. The holes can react either or adsorbed with surface hydroxyl to form hydroxyl radicals. As a result, the adsorption equilibrium is destroyed and dye molecules could move from solution to the interface and consequently decompose to CO<sub>2</sub>, H<sub>2</sub>O and other minerals through a redox reaction.



These are the some imprecise mechanism to photodegradation of the dyes and heavy metals. Photoelectrons used for degrading dyes must be accepted and delivered gone to resist the recombination of the photoelectrons and holes, which would give a higher efficiency of photocatalytic degradation. One more factor for the high performance of photocatalysts is that the Fe<sub>2</sub>O<sub>3</sub>/GO nanostructure and GO sheets can connect to each other with very tight bonding. Such a photocatalytic degradation process for dyes has been demonstrated to be an efficient approach to remove synthetic dye stuff from aquatic environments. The excellent photocatalytic activity of the Fe<sub>2</sub>O<sub>3</sub>-GO: 180 °C in Rhodamine B (RB) and Janus green (JG) in all conscientious 10, 20 and 30 ppm. The composites is attributed to the high specific surface area and the reduction of electron-hole pair recombination due to the introduction of GO. an increase in the surface area and porosity, and tapering of the band gap are confirmed by BET surface area measurement Thus, a large specific surface area is beneficial for absorbing more light and increasing the number of unsaturated surface co-ordination sites to improve the photocatalytic performance.

### 3.4. Anti-*Mycobacterium tuberculosis* activity

Humans have been in a constant battle with tuberculosis (TB). Currently, excessive use of antibiotics has resulted in the spread of multi-drug resistant *Mycobacterium tuberculosis* (MDR), leading to antibiotic ineffectiveness at controlling the spread of TB infection in host cells and especially macrophages. In addition, the *Mycobacterium tuberculosis* (*Mtb*) has developed methods to evade the immune system and survive. With the discovery of nanoparticle (NP) based drugs, it is necessary to assess their anti-mycobacterial properties and bactericidal mechanisms. In this study, we synthesized mixed metal oxide NPs and tested their ability to inhibit *Mtb* growth into macrophages.

Nano-sized particles were estimated at 13–17 nm, and the initial concentration of Fe<sub>2</sub>O<sub>3</sub>-GO: 140°C, Fe<sub>2</sub>O<sub>3</sub>-GO: 160°C, Fe<sub>2</sub>O<sub>3</sub>-GO: 180°C were estimated at 10 µg/ml. The minimal inhibitory concentration ratio of Fe<sub>2</sub>O<sub>3</sub>-GO: 140°C was detected in between 12.5 µg/ml to 100 µg/ml of the initial concentration to Fe<sub>2</sub>O<sub>3</sub>-GO: 160°C. Fe<sub>2</sub>O<sub>3</sub>-GO: 180°C and exhibit the 12.5 µg/ml potent antibacterial activity among the controllable composites. Fe<sub>2</sub>O<sub>3</sub>-GO nano-composites at all concentrations showed cytotoxic activity, even though, Fe<sub>2</sub>O<sub>3</sub>-

GO composites exhibited low cytotoxicity, they were unable to inhibit Mtb growth in vitro and exhibited strong anti-Mtb activity and inhibited bacterial growth, but exhibited high cytotoxicity to human macrophage cells, by Fe<sub>2</sub>O<sub>3</sub>-GO composites, we acquired a mixture that exhibited potent antibacterial activity against Mtb and no cytotoxic effects.

### *3.5. Measurement of growth-inhibitory effect of HEK-293 (human embryonic kidney – 293) cells against different Fe<sub>2</sub>O<sub>3</sub>-GO composite nanoparticles*

Functionalized Fe<sub>2</sub>O<sub>3</sub>-GO: 140°C, Fe<sub>2</sub>O<sub>3</sub>-GO: 160°C and Fe<sub>2</sub>O<sub>3</sub>- GO: 180°C was developed by using hydrothermal method to inhibit 50% of the proliferation of HEK-293 normal cells at 10 µg/mL concentration. This colorimetric assay is based on the capacity of mitochondria succinate dehydrogenase enzymes in living cells to reduce the yellow water-soluble substrate XTT into an insoluble, coloured formazan product, and therefore, this conversion only occurs in viable cells [27]. Additional incubation period for 4 hour after the addition of XTT labelling reagent, the change in the colour of the solution in different wells is observed. A solution of orange formazan is formed, which is quantified spectrophotometrically using an ELISA plate reader at 490 nm [28]. For this, a graph of absorbance against different concentrations of Fe<sub>2</sub>O<sub>3</sub>-GO was plotted and the inhibitory effect (IC<sub>50</sub>) was calculated. The reduction of XTT can only occur in metabolically active cells; the level of activity is a measure of viability of cells. Absorbance values that are lower than the control cell lines reveals decline in the rate of cell proliferation. In opposition, a higher absorbance indicates an increase in the cell proliferation. Untreated microtiter plates of cell lines with only medium (0.3% v/v DMSO in water) is considered as proliferative control. An increase in number of living viable cells results in an increase in the total activity of mitochondrial dehydrogenases in the anti-malignant cells. As observed by the absorbance, the increase is directly proportional to the orange formazan formed quantitatively [29]. This process is safe, unlike available other alternatives, as no radioactive isotopes are used. The results found are precise and can be correlated to the number of viable cell number. The method is also sensitive and can be used for large number of samples. The inhibition of cell proliferation percentage by the Fe<sub>2</sub>O<sub>3</sub>-GO with different controllable synthesis was calculated based on difference in inhibitory effect between treated cell lines and their respective controls.

The prominent anti-proliferative effect of functionalized Fe<sub>2</sub>O<sub>3</sub> /GO: 140 °C, 160 °C and 180 °C on HEK-293 as revealed by its IC<sub>50</sub> based on XTT assay was found to be 216.78 ± 0.32, 185.32 ± 0.41, and 196.15 ± 0.26 respectively. IC<sub>50</sub> of 185.32 ± 0.41 in Fe<sub>2</sub>O<sub>3</sub> /GO: 160 °C is shows a minimum activity, compared to the in-organic drug Cisplatin >500 used as standard drug for these study in Table 5. Therefore, it can be said that Fe<sub>2</sub>O<sub>3</sub> /GO: 160°C is a promising candidate for anti-cancer face. However, the synthesis mechanism behind the anti-proliferative effects of Fe<sub>2</sub>O<sub>3</sub>/GO controllable composites needs to be studied to determine whether the effect is due to an increase in apoptosis. The plasma membrane of the cell defines the separation between the internal constituents of a cell and the outside environment. This semi-permeable membrane allows free diffusion of small and non-polar molecules. However, bigger ones like nanomaterials are incapable of crossing the plasma membrane which requires uptake mechanisms such as endocytosis. Most of chemically functionalized Fe<sub>2</sub>O<sub>3</sub> /GO are easily taken up by the cells through endocytotic mechanisms, but they remain in endosome vesicles, and become incapable of reaching the cytosol system. Although endocytotic uptake is the normal phenomenon for a variety of nanomaterials, the efficiency predominantly depends on shape, size, the dispersivity nature and the other physico-chemical parameters. This is important, because there may be many factors that affect the anti-proliferative activity in the *in vivo* study. Further study is started. Table 5 shows growth of inhibitory effect of functionalized Fe<sub>2</sub>O<sub>3</sub>-GO on HEK-293 cell lines, is evident that, hydrothermally synthesized composite metal oxides with controllable sizes can be used effectively at a very low concentration against different types of cell lines for the drug delivery procedures and also, pharmaceutical applications.

## **4. Conclusions**

In summary, controllable synthesis of Fe<sub>2</sub>O<sub>3</sub>/GO wrapped nanocomposite by a facile hydrothermal method and characterization of synthesized materials were carried out by using advanced instruments. The synthesized materials were screened for anti-microbial and anti-TB activity and found-excellent activity, and in particular concentration they are non-toxic to the normal cell lines. The synthesized composite also studied for substantial applications such as, heavy metal and dye degradation and nano-composite exhibited the highest photocatalytic activity. Finally, our work not only paves a new way for the controllable growth of high quality of metal oxides composite but also, has a multifunctional application with an eco-friendly label. Composite material size, size distribution, and shape of Fe<sub>2</sub>O<sub>3</sub>/GO wrapped composites are the important parameters influencing the environmental degradation and bio-sharing in-vitro applications.

## Conflicts of interest

There are no conflicts to declare.

## Acknowledgement

The first author Abhilash M R (IF160104) is thankful to the Department of Science and Technology, Govt. of India, New Delhi, for awarding the financial assistance through DST – *INSPIRE* Junior Research Fellowship to carry out the research in the University of Mysore, Mysuru – 570 006, Karnataka, India.

## References

- W. Wu, Q. G. He, C. Z. Jiang, Magnetic iron oxide nanoparticles: synthesis and surface functionalization strategies, *Nanoscale Res. Lett.* 3, (2008) 397-407.
- L. Yang, Development of receptor targeted magnetic iron oxide nanoparticles for efficient drug delivery and tumour imaging, *J. Biomed Nanotechnol.* 4, (2008) 439-449.
- A. H. Lu, E. L. Salabas, F. Schuth, Magnetic nanoparticles; synthesis, protection, fictionalization and application, *Angew Chem Int. Edn.* 46, (2007) 1222-1241.
- W. Wu, X. H. Xiao, S. F. Zhang, T. C. Peng, J. Zhou, F. Ren , C. Z. Jiang, Synthesis and magnetic properties of maghemite ( $\gamma$ -Fe<sub>2</sub>O<sub>3</sub>) short-nanotubes, *Nanoscale Res. Lett.* 5, (2010) 1474-1482.
- S. Hui, Y. Zhibin, H. Nuri, High-performance iron oxide-graphene oxide nanocomposite adsorbents for arsenic removal, *Colloids and Surfaces.* (2017) 1, 261–272.
- K. Byrappa, K. Namratha, S. M. Byrappa, Hydrothermal Growth of Crystals—Design and Processing, In the Book: *Handbook of Crystal Growth*, Second Edition. (2005) 2, 535-575.
- D. C. Marcano, D. V. Kosynkin, J. M. Berlin Sinitskii, A. Z Sun, A. Slesarev, L.B. Alemany, W. Lu, J.M. Tour, *ACS Nano.* (2010) 1, 4806-4814.
- CLSI, Performance Standards for Antimicrobial Disk Susceptibility Tests, Approved Standard (CLSI DocumentM02-A11), Clinical and Laboratory Standards Institute USA, (2012). Seventh ed.,
- CLSI, Methods for Dilution Antimicrobial Susceptibility Tests for Bacteria that Grow Aerobically, Approved Standard, CLSI document M07-A9, Clinical and Laboratory Standards Institute, 950 West Valley Road, Suite 2500, Wayne, Pennsylvania 19087. USA, (2012). Ninth ed.,
- X. Chen, X. Huang, C. Zheng, Y. Liu, T. Xu, J. Liu, Preparation of different sized nano-silver loaded on functionalized graphene oxide with highly effective antibacterial properties, *J. Mat. Chem.* 35 (3), (2015) 7020-7029.
- C. S. Maria, V. Lourenco Marcus, N. de Souza, C. Alessandra Pinheiro, L. Marcelle de. Ferreira, B. Rasnisb, Goncalves, M. Thais Cristina Nogneira, A. Monica Peralta, Evaluation of anti-Tubercular activity of nicotinic and isoniazid analogues, *ARKIVOC.* 15, (2007) 181-191.
- L. Xu, J. W. Mc Graw, F. Gao, M. Grundy, Z. Ye, Z. Gu, J. L. Shepherd, Production of high-concentration graphene dispersions in low-boiling-point organicsolvents by liquid-phase noncovalent exfoliation of graphite with ahyperbranched polyethylene and formation of graphene/ethylene copolymercomposites, *J. Phys. Chem. C.* 117, (2013) 10730-10742.
- T. Taniguchi, K. Nakagawa, T. Watanabe, N. Matsushita, M. Yoshimura, Hydrothermal growth of fatty acid stabilized iron oxide nanocrystals, *J. Phys. Chem.* 113, (2009), 839-843.
- P. Tartaj, M. Del Puerto Morales, S. Veintemillas Verdaguera, T. Gonzalez Carreno, J. C Serna, The preparation of magnetic nanoparticles for applications in biomedicine, *J. Phys. D: Appl. Phys.* 36, (2003) R182-R197.
- S. Laurent, D. Forge, M. Port, A. Roch, R. N. Robic, Muller, Magnetic iron oxide nanoparticles, *Chem. Rev.* 108, (2008) 2064-2110.
- S. Luther, N. Borgfeld, J. Kim, J. G. Parsons, Removal of arsenic from aqueous solution: a study of the effects of pH and interfering ions using iron oxide nanomaterials, *J. Microchem.* 101 (2012) 30-36.
- M. Baikousi, A. B Bourlinos, A. Douvalis, T. Bakas, D. F. Anagnostopoulos, J. Tucek, K. Safarova, R. Zboril, M. A. Karakasside, Synthesis and characterization of  $\gamma$ -Fe<sub>2</sub>O<sub>3</sub>/carbon hybrids and their application in removal of hexavalent chromium ions from aqueous solutions, *Langmuir.* 28, (2012) 3918-3930.
- V. Chandra, J. Park, Y. Chun, J. W. Lee, I. C. Hwang , K. S. Kim, Water dispersible magnetite-reduced graphene oxide composites for arsenic removal, *ACS Nano.* 4, (2010) 3979-3986.
- K. S. W. Singh, D. H. Everett, R. A. W. Haul, L. Moscou, R. A. Pierotti, J. Rouquerol, T. Siemieniewska, Reporting physic-sorption data for gas/solid systems with special reference to the determination of surface area and porosity, *Pure Appl.Chem.* 57, (1985) 603-619.
- S. Yean, L. Cong, C. T. Yavuz, J. T. Mayo, W. W. Yu, A. T. Kan, V. L. Colvin, M. B. Tomson, Effect of magnetite particle size on adsorption and desorption of arsenite and arsenate, *J. Mater. Res.* 20, (2005) 3255-3264.
- J. D. Clogston and A. K. Patri, Zeta potential measurement, *Meth. Mol. Biol.* 697, (2011) 63-70.
- Y. F. Sun, H. Cheng, S. Gao, Z. H. Sun, Q. H. Liu, Q. Liu, F. C. Lei, T. Yao, J. F. He, S. Q. Wei, Y. Xie, Freestanding tin disulfide single-layers realizing efficient visible-light water splitting, *Angew. Chem Int Ed.* 51, (2012) 8727-8737.

23. B. Seger, A. B. Laursen, P. C. K. Vesborg, T. Pedersen, O. Hansen, S. Dahl, I. Chorkendorff, Hydrogen production using a molybdenum sulfide catalyst on a titanium-protected n+p-silicon photocathode, *Angew Chem Int Ed.* 51, (2012) 9128-9139.
24. L. Zhu, Z. D. Meng, M. L. Chen, F. J. Zhang, J. G. Choi, J. Y. Park, W. C. Oh, Preparation, characterization and photocatalytic behavior of  $\text{WO}_3$ -fullerene/ $\text{TiO}_2$  catalysts under visible light, *J. Photocatal. Sci.* 1, (2010) 69-76.
25. Q. Xiang, J. Yu and M. Jaroniec, Graphene-based semiconductor photocatalysts, *Chem. Soc. Rev.* 41, (2012) 782-796.
26. Y. Zhang, N. Zhang, Z. R. Tang, Y. J. Xu, Graphene Transforms Wide Band Gap ZnS to a Visible Light Photocatalyst. The New Role of Graphene as a Macromolecular Photosensitizer, *ACS Nano.* 6, (2012), 9777-9789.
27. M. V. Berridge, A. S. Tan, K. D. Mccoy, R. Wang, The biochemical and cellular basis of cell proliferation assays that use tetrazolium salts, *Biochemica.* 4, (1996) 14-19.
28. S. Sacconi, D. Simkin, N. Arrighi, F. Chapon , M. M. Larroque, S. Vicart, D. Sternberg, B. Fontaine, J. Barhanin, C. Desnuelle, S. Bendahhou, Mechanisms underlying Andersen's syndrome pathology in skeletal muscle are revealed in human myotubes, *Am J Physiol Cell Physiol.* 297, (2009) C876-C885.,
29. N. Leviar, R. A. Dewey, E. Daley, T. E. Bates, D. Davies, J. Kos, G. J. Pilkington, T. T. Lah, Selective suppression of cathepsin L by antisense c DNA impairs human brain tumor cell invasion in vitro and promotes apoptosis, *Canc Gene Ther.* 10, (2003) 141-151.

**Table.1.** Particle sizes and Magnetic properties of  $\text{Fe}_2\text{O}_3$ /GO nanoparticles synthesized at different reaction temperature.

Composite	Reaction Temperature (12 h)	Particle Sizes $d_{xrd}$ (nm)	Magnetic Results		
			$M_s$ (emu/g)	$H_c$ (Oe)	$H_s$ (Oe)
$\text{Fe}_2\text{O}_3$ /GO	140 °C	13	81.0	89	8.158
$\text{Fe}_2\text{O}_3$ /GO	160 °C	15	78.2	72	8.651
$\text{Fe}_2\text{O}_3$ /GO	180 °C	17	75.6	38	8.452

**Table.2.** Results from  $\text{N}_2$  sorption Characterization

Sample	Surface area ( $\text{m}^2\text{g}^{-1}$ ) <sup>a</sup>					Pore volume ( $\text{cm}^3\text{g}^{-1}$ ) <sup>b</sup>					$D_{meso/macro}$
	$S_{BET}$	$S_{d=20\text{\AA}}$	% $S_{d=20\text{\AA}}$	$S_{d>20\text{\AA}}$	% $S_{d>20\text{\AA}}$	$V_{total}$	$V_{d=20\text{\AA}}$	% $V_{d=20\text{\AA}}$	$V_{d>20\text{\AA}(des)}$	% $V_{d>20\text{\AA}}$	
GO	126	87	49%	44	34%	0.09	0.05	53%	0.04	47%	27
$\text{Fe}_2\text{O}_3$ -GO, 140°C	347	145	40%	198	60%	0.20	0.07	35%	0.13	65%	6
$\text{Fe}_2\text{O}_3$ -GO, 160°C	352	77	24%	248	76%	0.21	0.04	20%	0.17	80%	6
$\text{Fe}_2\text{O}_3$ -GO, 180°C	354	31	11%	301	89%	0.29	0.02	7%	0.27	93%	7
$\text{Fe}_2\text{O}_3$	75	1.5	2%	74	98%	0.36	0.00	0%	0.36	100%	28

<sup>a</sup> BET surface area ( $S_{BET}$ ), surface area of micropores ( $S_{d<20\text{\AA}}$ ) and surface area of meso-/macro pores ( $S_{d>20\text{\AA}}$ ) determined with the t-plot method.

The percentage data denotes the percentage of surface area of micropores or meso- and macropores relative to the total surface area.

<sup>b</sup> Total pores volume ( $V_{total}$ ), micro volume ( $V_{d<20\text{\AA}}$ ) determined with the t-plot method. The percentage data denote the percentage of pore volume of micropores relative to the total pore volume.

<sup>c</sup> Average meso-/macropores size ( $D_{meso/macro}$ ) determined from the  $\text{N}_2$  desorption data with NLDET model.

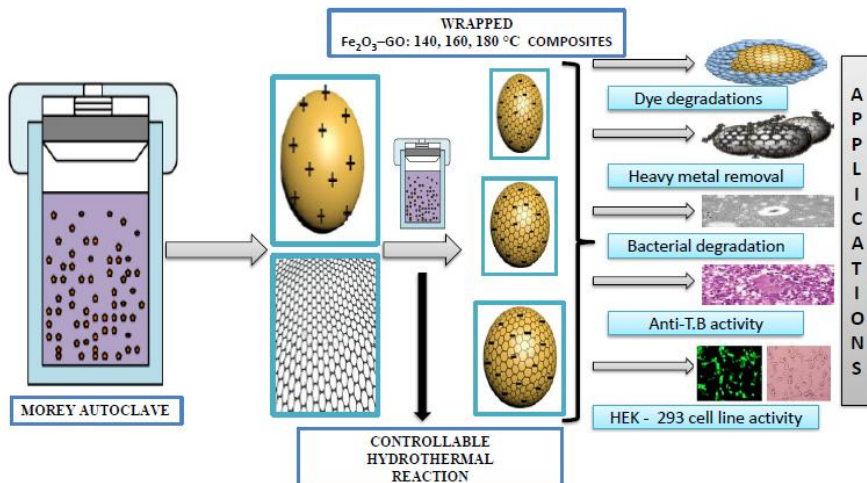
**Table.3.** Antibacterial activity of  $\text{Fe}_2\text{O}_3$ -GO nano-composite against test pathogens.

Test Sample	Zone of inhibition (in mm)			
	<i>B. subtilis</i>	<i>Staph. aureus</i>	<i>P. aeruginosa</i>	<i>E. coli</i>
$\text{Fe}_2\text{O}_3$ -GO: 140 °C	$09.23 \pm 0.14$	$14.13 \pm 0.11$	$17.09 \pm 0.32$	$15.60 \pm 0.11$
$\text{Fe}_2\text{O}_3$ -GO: 160 °C	$03.53 \pm 0.11$	$17.24 \pm 0.33$	$19.24 \pm 0.12$	$17.41 \pm 0.06$
$\text{Fe}_2\text{O}_3$ -GO: 180 °C	$02.22 \pm 0.24$	$23.24 \pm 0.33$	$22.10 \pm 0.23$	$20.17 \pm 0.07$
Std. DW	$00.00 \pm 0.00$	$00.00 \pm 0.00$	$00.00 \pm 0.00$	$00.00 \pm 0.00$

**Note:** Values are means of three independent replicates;  $\pm$  indicate standard error. Means followed by the same letter(s) within the same column are not significantly different according to Tukey's HSD.

**Table 4.** Inhibitory concentration values ( $IC_{50}$ ) of HEK-293 (human embryonic kidney – 293) cells against different  $Fe_2O_3$ -GO composite nanoparticles.

Controllable Composite	$IC_{50}$ ( $\mu$ g/ml)
$Fe_2O_3$ /GO: 140 °C	$216.78 \pm 0.32$
$Fe_2O_3$ /GO: 160°C	$185.32 \pm 0.41$
$Fe_2O_3$ /GO: 180 °C	$196.15 \pm 0.26$
STD (Cisplatin)	>500



**Scheme 2.** Schematic design of  $Fe_2O_3$ -GO wrapped composite by hydrothermal processes and applications

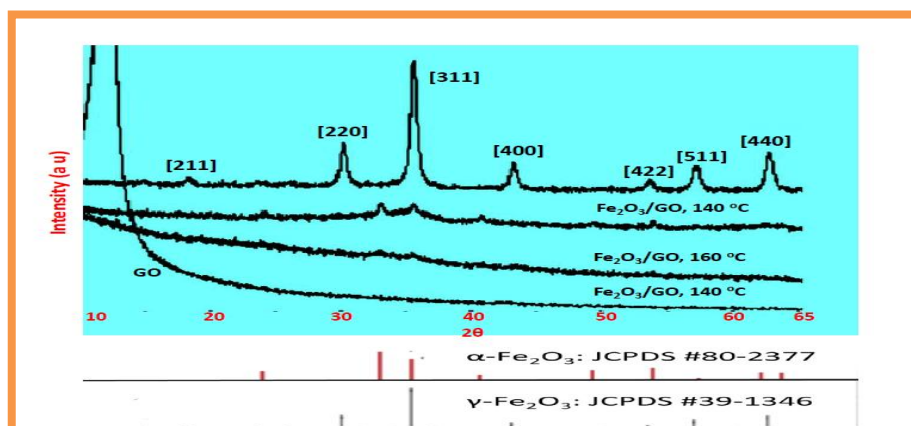


**Figure 1.** X-Ray Diffraction profile of GO,  $Fe_2O_3$ -GO: 140°C,  $Fe_2O_3$ -GO: 160°C,  $Fe_2O_3$ -GO: 180°C.

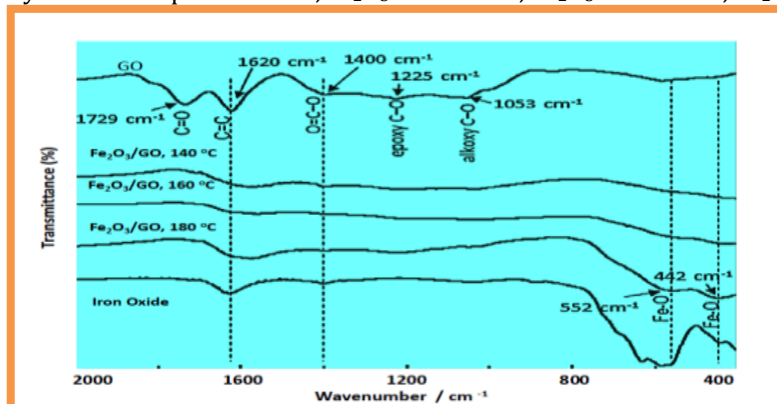


**Figure 2.** FT-IR spectra of GO,  $Fe_2O_3$  and  $Fe_2O_3$ -GO: 140°C,  $Fe_2O_3$ -GO: 160°C,  $Fe_2O_3$ -GO: 180°C controllable composites.

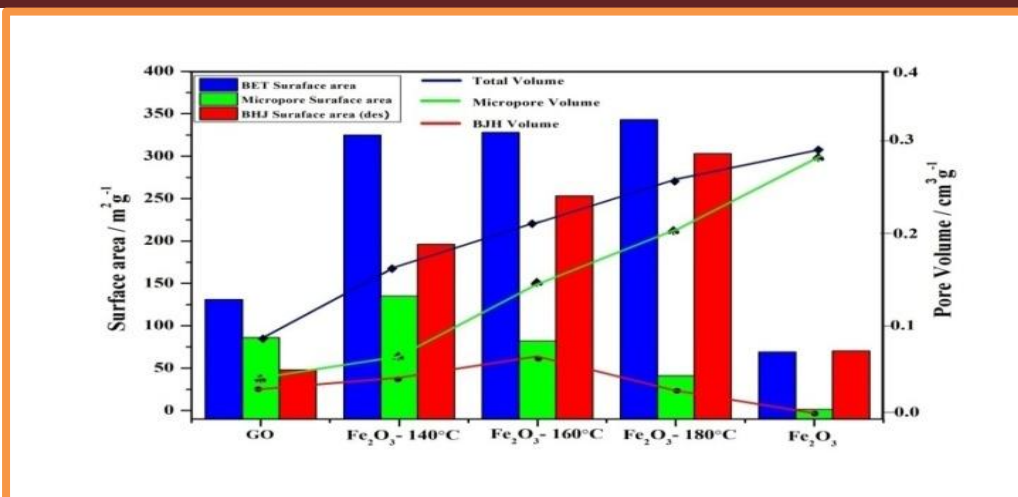


**Figure. 3.** Dependencies of surface area and pore volume data on the  $\text{Fe}_2\text{O}_3$ /GO composites.

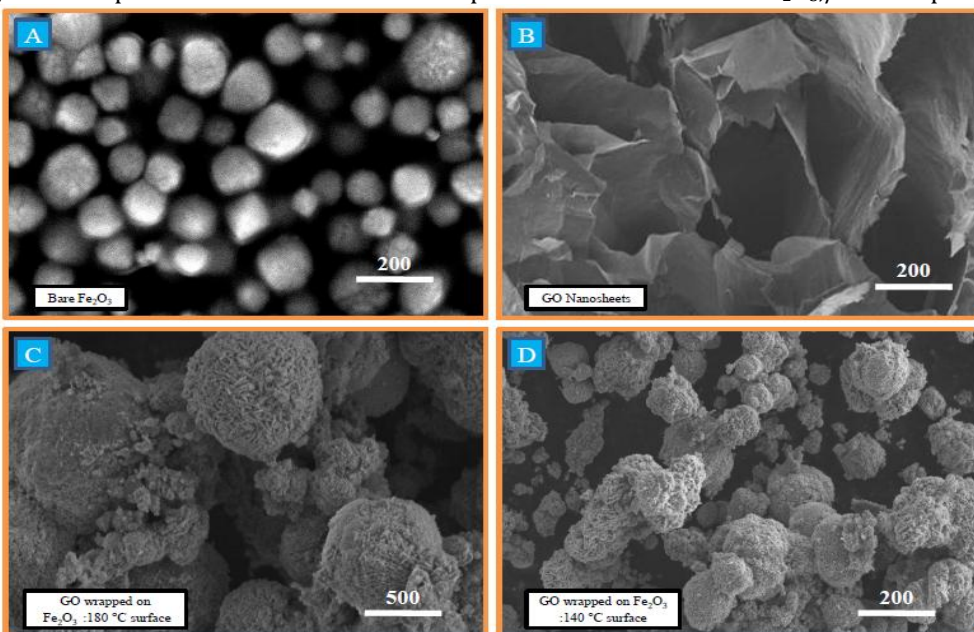


**Figure. 5.** Scanning Electron Microscopic images of A.  $\text{Fe}_2\text{O}_3$  nanoparticles, B. GO nanosheets, C. GO wrapped on  $\text{Fe}_2\text{O}_3$  surface at 180°C, D. Progressively GO wrapped on 140°C  $\text{Fe}_2\text{O}_3$  surface.

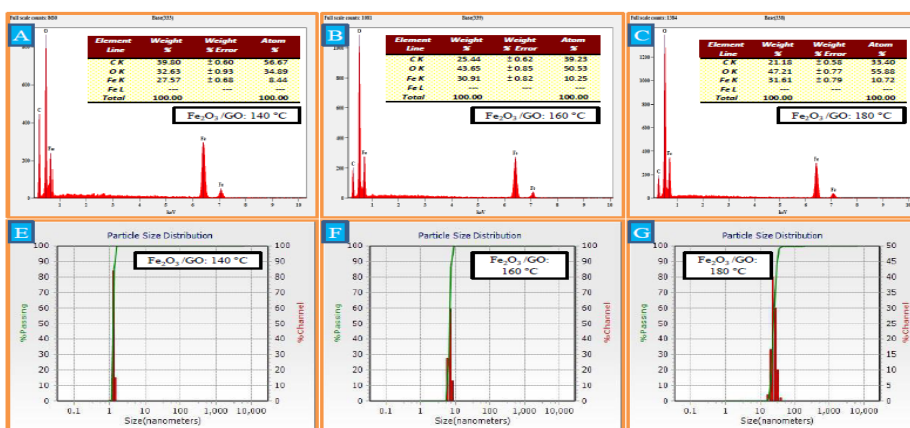


**Figure. 6.** The elemental composition and atomic percentage in EDS and evaluating particle size, distribution and zeta potential DLS results of A – E.  $\text{Fe}_2\text{O}_3$ -GO: 140°C, B – F.  $\text{Fe}_2\text{O}_3$ -GO: 160°C and C – G.  $\text{Fe}_2\text{O}_3$ -GO: 180°C.

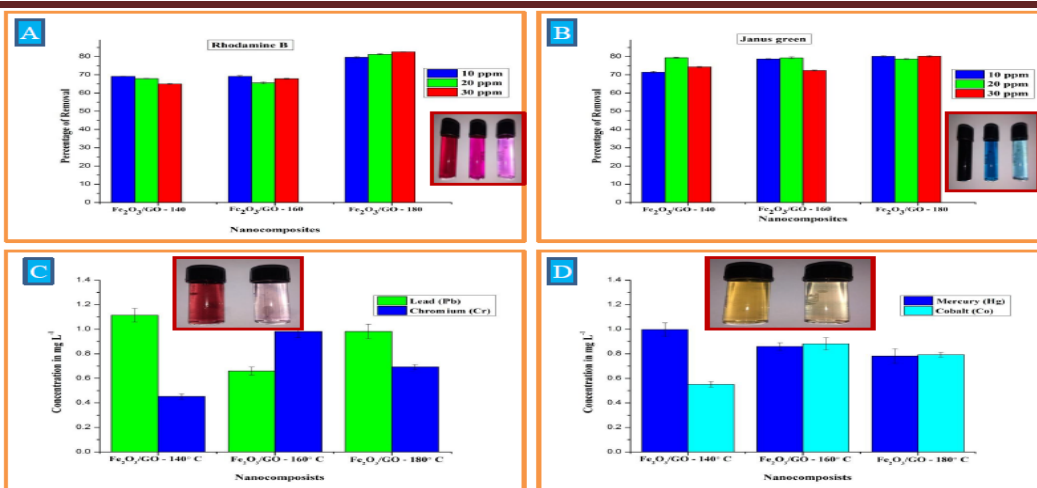


**Figure 7.** Fraction removal of dye concentration of A. Rhodamine B (RB) and B. Janus green (JG), similarly, Heavy metal degradation efficiency of C. Lead (Pb); Chromium (Cr) and D. Mercury (Hg); and Cobalt (Co).

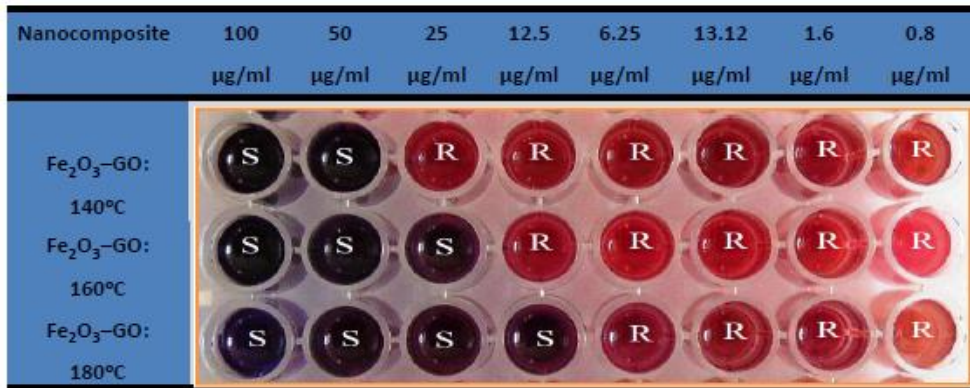


**Figure 8.** The results of anti-mycobacterial tests (MIC) with different dilution of  $\text{Fe}_2\text{O}_3-\text{GO}$ :  $140^\circ\text{C}$ ,  $\text{Fe}_2\text{O}_3-\text{GO}$ :  $160^\circ\text{C}$ ,  $\text{Fe}_2\text{O}_3-\text{GO}$ :  $180^\circ\text{C}$  in contraction with Mycobacterium tuberculosis (H37-Rv Mbt)

**Note:** S - Sensitive R - Resistant Strain used: *M. tuberculosis* (H37 RV strain): ATCC No- 27294. Here are the standard values for the Anti-Tb test which was performed. Pyrazinamide -  $3.125\mu\text{g}/\text{ml}$ , Streptomycin- $6.25\mu\text{g}/\text{ml}$  and Ciprofloxacin- $3.125\mu\text{g}/\text{ml}$